Wideband dual-polarized hollow-waveguide slot array antenna

You, Qingchun; Wang, Yi; Huang, Mingjian; Huang, Jifu; Zheng, Zi-wei; Lu, Yunlong

DOI:
10.1109/TAP.2022.3184544

Wideband Dual-Polarized Hollow-Waveguide Slot Array Antenna

Qingchun You, Yi Wang, *Senior Member, IEEE*, Mingjian Huang, Jifu Huang, Zi-Wei Zheng, and Yunlong Lu, *Member, IEEE*

***Abstract*— A wideband dual-polarized slot array antenna based on hollow-waveguide is presented in this paper. Its wide bandwidth and high performance are enabled by two separate feeding networks, from the side and the bottom, using square coaxial line and ridge waveguide structures, respectively. The full-corporate-feed networks excite the radiation slots in a one-to-one fashion without using backed cavities. Tight element spacing is made possible, suppressing the grating lobe and maintaining high cross polarization discrimination (XPD) across the wideband. This resolves a usual trade-off between bandwidth and grating lobe. A double-ridge rectangular waveguide cavity is devised as an orthogonal mode splitter for isolation enhancement. Several design features are used to minimize the signal path length and facilitate routing. An 8×8-element prototype in K-band is designed, fabricated, and measured. Experimental results show that the antenna has a wide bandwidth of 23.4% (from 17 – 21.5 GHz) free from grating lobes. More than 25.5 dBi peak gain, higher than 51.2 dB isolation and over 43.6 dB XPD are also obtained for the dual polarizations.**

Keywords—*Dual-polarization array antenna, waveguide antenna, wideband, high isolation, low cross polarization.*

I. Introduction

With the emergence of new applications, such as the Internet of Things (IoT) and AR/VR, the demand for wireless communication capacity is rapidly increasing [1]-[3]. Wideband dual-polarized antennas are highly desired, as they can combat multipath fading by polarization diversity and improve channel capacity [4]-[7]. Microstrip lines and substrate-integrated waveguides (SIWs) have been commonly used to realize dual-polarized antennas and arrays, where most work focused on the bandwidth, isolation and cross polarization discrimination (XPD) [8]-[15]. However, these antennas are often limited in their efficiency and gain due to high dielectric loss, especially in a high microwave band. In long-distance wireless communication scenarios, wideband, high-gain and high-efficiency array antennas are required for establishing stable communication links [16]-[18]. Dual-polarized antennas implemented by using low-loss solutions become attractive. Parabolic reflectors and reflectarrays are a common choice because of their advantages of low cost and ease of manufacturing [19]-[24]. However, these types of antennas are generally bulky with a large profile, which is a major shortcoming.

As a competitive alternative, hollow-waveguide (HW) slot array antenna can offer a compact and planar formfactor with high-efficiency [25]-[28]. Some HW-based dual-polarization slot array antennas have been reported [29]-[36]. There are two feeding methods. One is based on the series (or partial series) feed structure. The two typical designs are: (i) to excite orthogonally placed continuous transverse stub array or cross-slot array in series [29]-[31], or (ii) to excite the combination of V-shaped and offset longitudinal slots with partial-series feed network [32]-[34]. The fractional bandwidth (FBW) of this type of dual-polarized antennas is relatively narrow, usually within 10%.

The other method is based on a full-corporate-feed network. There have been some recent examples with impressive performance. Cross-shaped slot, square-shaped slot or magneto-electric (ME) dipole have been used to achieve dual polarization [35]-[37]. To facilitate the layout of the feed network, 1-to-4 backed cavity has been used to excite the 2×2-element sub-array in all these works. For the consideration of grating lobe suppression in the E-/H- and diagonal planes, the period between the array elements in the concerned planes should be as small as possible (preferably smaller than one free-space wavelength at the highest operation frequency). To meet this requirement, the backed cavity must be constrained to operating in the fundamental mode to reduce the cavity size. However, this adversely limits the achievable FBW to less than 20% [37]. In addition, the use of common backed cavity [35] to excite two polarizations increases the risk of cross-polarization deterioration. The FBW can be enhanced by increasing the backed cavity size as demonstrated in [37]. The FBW of 26.3% has been obtained. However, an unfavorable consequence is the significantly deteriorated grating lobe level (to about -13 dB) due to the increased space between the radiation elements.

Some efforts have been made to overcome this shortcoming by eliminating the 1-to-4 backed cavity in dual-polarized array antennas [38], [39]. However, the removal of the cavity makes the feed network more complicated, which in turn makes it

This work was supported partly by National Natural Science Foundation of China under Projects 62171242, U1809203, and 61631012, in part by Zhejiang Provincial Natural Science Foundation of China under Project LY21F010002. (*Corresponding author: Yunlong Lu*)

Qingchun You, and Yi Wang are with School of Engineering, University of Birmingham, B15 2TT, United Kingdom (e-mail: y.wang.1@bham.ac.uk).

Mingjian Huang, Jifu Huang, and Yunlong Lu are with the Faculty of Electrical Engineering and Computer Science, Ningbo University, Ningbo, Zhejiang, 315211, China (e-mail: luyunlong@nbu.edu.cn).

Zi-Wei Zheng is with Digital Industry Research Institute, Zhejiang Wanli University, Ningbo, Zhejiang, 315100, P. R. China

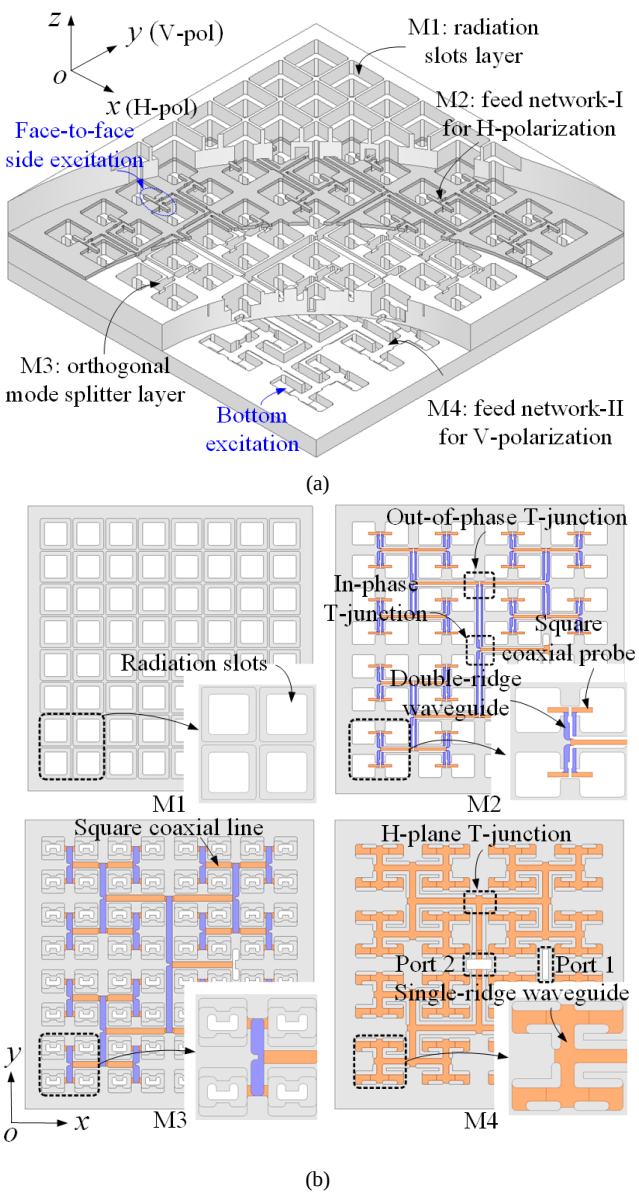

Fig. 1. Configuration of the dual-polarized array antenna. (a) 3-D view; (b) separated metal layers.

more difficult to reduce the period between array elements. [39] reported an 8×8 full-corporate-feed dual-polarized slot array antenna without the backed cavities. The antenna has good radiation pattern envelope, low cross-polarization pattern and high isolation. However, due to the size restriction of the gap ridge waveguide, the space between the adjacent slots is only reduced to about one free-space wavelength at the center frequency. Coupled with the limited bandwidth of the orthogonal mode splitter (based on a coupling slot structure), the FBW of this antenna is only about 5%. How to increase the bandwidth of HW-based dual-polarized array antennas without sacrificing their key performance remains a significant design challenge.

This work aims to tackle this challenge by applying a number of new design features: (i) A new array element structure is proposed, with a stepped square-shaped radiation slot, fed from the side and the bottom, which enables a wideband impedance matching for the dual polarizations. (ii) Double-ridge waveguide cavities are devised to function as the orthogonal mode splitter to improve the port isolation over a wide frequency band. (iii) As the key contribution of this work, two sets of wideband full-corporate-feed networks with different transmission structures (square coaxial line and ridge waveguide, respectively) are used to excite the radiation slots for the two polarizations on a one-to-one basis. This topology eliminates the 1-to-4 backed cavities in the conventional designs, overcoming the performance constraints caused by these cavities, in terms of bandwidth, grating lobes and cross polarization discrimination (XPD). With these new features, the proposed array antenna exhibits wide impedance bandwidth free from grating lobe, high antenna efficiency, high isolation and XPD. The paper is organized as follows: Section II describes the antenna configuration. Section III and IV present the analysis, design, and results followed by conclusion in Section V.

II. Antenna Configuration

Fig. 1(a) shows the 3D view of the proposed dual-polarized antenna array. The concerned frequency band is 17- 21.5 GHz. It is based on HW to avoid the dielectric loss. It consists of 8×8 stepped square-shaped radiation slots excited with two separate full-corporate-feed networks. The antenna array is a multilayer structure. Considering the manufacturability, it is divided into four layers. They are the radiation slot layer M1, the first full-corporate-feed network I for H-polarization (H-pol) in M2, the orthogonal mode splitter layer in M3, and the second full-corporate-feed network II for V-polarization (V-pol) in M4. The structure of each layer is shown in Fig. 1(b). Note that the feed network-I is a hybrid structure of double-ridge waveguides and square coaxial line, while the feed network-II is only based on the single-ridge waveguide. The 1-to-4 power divider units in the feed networks I and II are discussed in section III-B. Two standard waveguide input ports are located at the back side of the antenna for the two polarizations.

Different from the previous works in [35]-[37], 1-to-4 backed cavity layer is eliminated to avoid its drawbacks as discussed in Introduction. Instead, the radiation slots are excited by the two separate feed networks in a one-to-one correspondence. Compared with the work in [39], the spaces between adjacent elements in *x*- and *y*-directions are reduced. The FBW of the proposed antenna is broadened (See in Section III). All the simulation results are performed by using Ansoft HFSS. The detailed design and analysis of the array element, the 2×2-element sub-array and the whole antenna will be presented in the following sections.

III. Analysis and Design

The configuration of the 2×2-element sub-array, as well as the enlarged view of the corresponding feed networks, are shown in Fig. 2. Periodic boundaries are used in the simulations for considering the mutual coupling among the sub-arrays. To avoid the grating lobes in the desired frequency band, the period (*d*) between the adjacent elements along both *x*- and

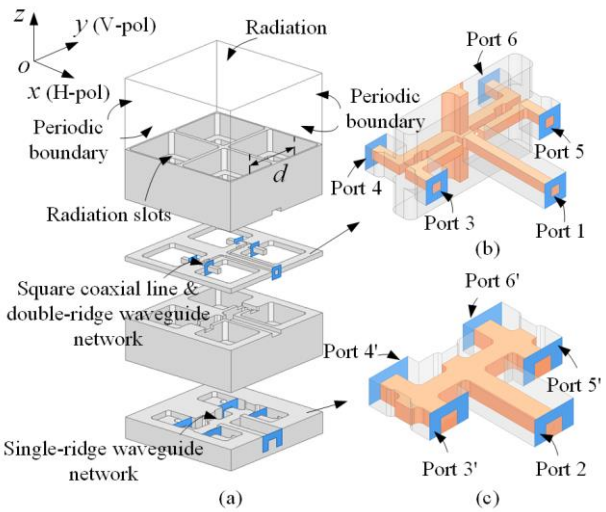

Fig. 2. Configuration of the 2×2-element dual-polarized sub-array. (a) Whole structure; (b) feed network for H-pol; (c) feed network for V-pol.

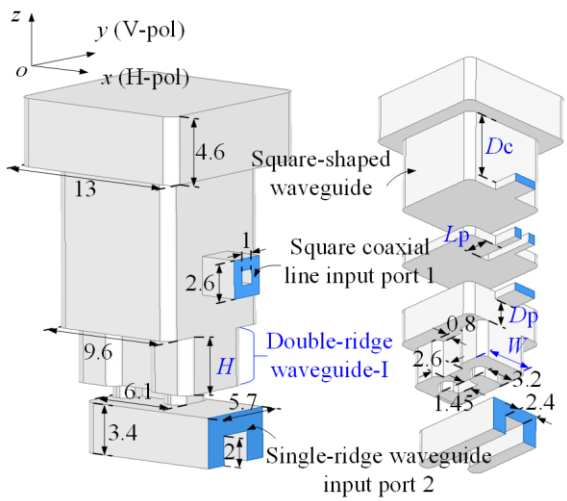

Fig. 3. Air model of the array element. All dimensions are given in millimeters.

y-directions is less than one free-space wavelength at the highest operating frequency. It is d = 13.8 mm in this design, slightly smaller than the free-space wavelength at 21.5 GHz. As aforementioned, two different feed structures (coaxial line versus waveguide) in different metal layers are employed for the two polarizations. The feed network for the H-pol excites the square-shaped slots from the side, whereas the V-pol feed network excites from the bottom layer. The details of the array element and feed network are discussed in the following section A and B. It is noted that the array element is designed and optimized in the sub-array.

A. Array Element

The array element is a stepped square-shaped radiation slot with two feeding point at the side and bottom, as shown in Fig. 3. The stepped square-shaped slot offers the wide bandwidth and high antenna aperture efficiency. The side-feed (port 1) is based on a square coaxial line to generate the H-pol, while allowing a compact layout of the feed network. D_c is the distance from the feeding position to the top of the smaller square slot. Fig. 4(a) shows the amplitude distribution of

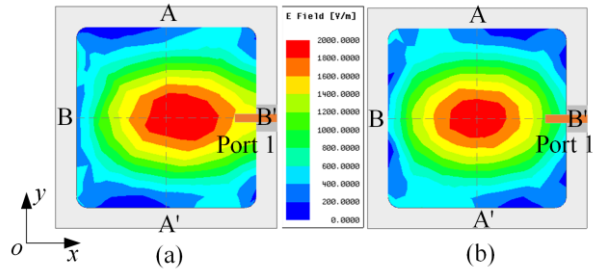

Fig. 4. Amplitude distribution of E-field at the radiation slots. (a) D_c= 2.6 mm; (b) D_c=6.6 mm.

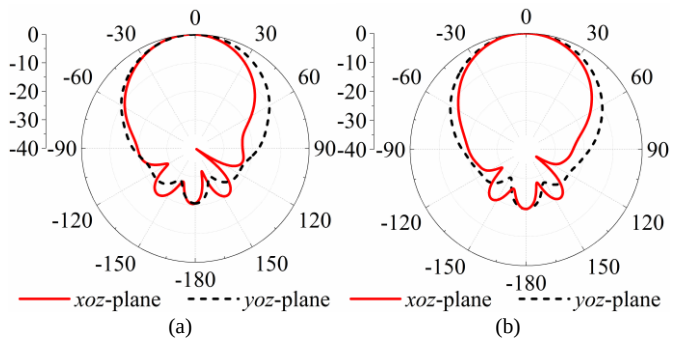

Fig. 5. Simulated radiation patterns of the array element with port 1 excitation at 19.5 GHz. (a) D_c= 2.6 mm; (b) D_c=6.6 mm.

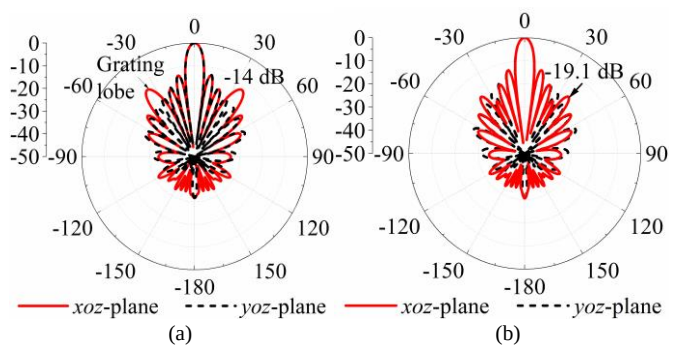

Fig. 6. Simulated radiation patterns of the 8×8-element array with port 1 excitation at 19.5 GHz. (a) D_c= 2.6mm; (b) D_c=6.6 mm.

E-field with D_c = 2.6 mm. The amplitude distribution is symmetrical along the plane B-B', but asymmetrical along the plane A-A' due to the asymmetry of the side feed. The region close to the side with the port 1 has more energy. This uneven amplitude distribution would lead to asymmetry radiation patterns in *xoz*-plane as opposed to the symmetry pattern in *yoz*-plane. The simulated results at 19.5 GHz in Fig. 5(a) confirm this phenomenon. Furthermore, this will also cause grating lobes when an array is formed. Fig. 6(a) plots the synthesized radiation patterns of a 8×8-element array antenna based on this unit structure (without feed network and with port 2 terminated with 50 Ω load). The grating lobes, with a level of -14 dB, appears at θ=± 36° in *xoz*-plane. An effective way to solve this asymmetry problem is to increase D_c so that only the fundamental mode is allowed to propagate while the higher order modes are attenuated. Fig. 4(b) shows the amplitude distribution of E-field when the D_c is increased to 6.6 mm. A more symmetric amplitude distribution can be achieved. Fig. 5(b) and Fig. 6(b) show a more symmetric radiation pattern which is then translated into lower side lobe of under -19.1 dB.

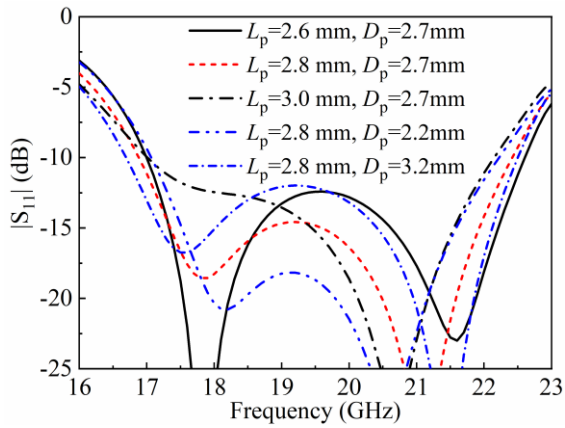

Fig. 7. Simulated $|S_{11}|$ of port 1 with different values of L_p and D_p.

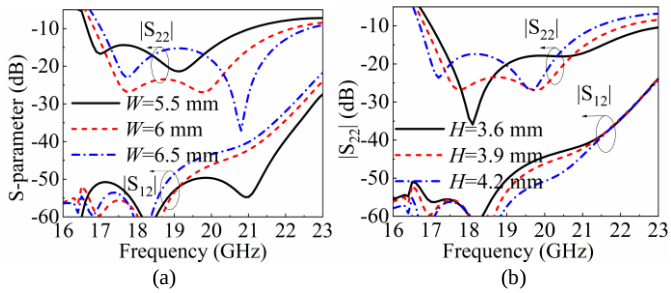

Fig. 8. Simulated $|S_{22}|$ of port 2 and isolations with different values of (a) W and (b) H.

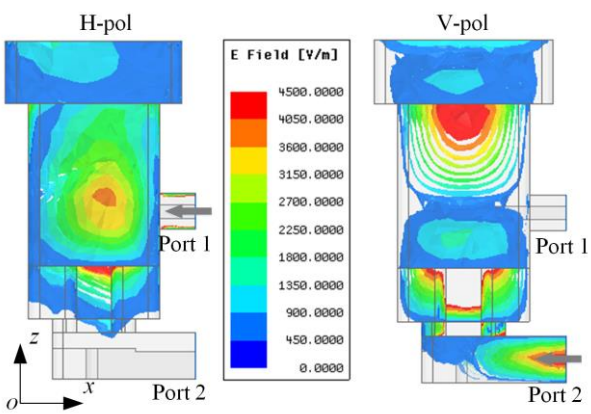

Fig. 9. Simulated E-field within the element when port 1 (left) and port 2 (right) is excited at 19.5 GHz.

The lower feeding structure for port 2 (V-pol) is based on a single-ridge waveguide. It is transitioned into a vertical double-ridge rectangular waveguide to excite the radiation slots. It is important to note that the double-ridge waveguide-I (see in Fig. 3) serves as the orthogonal mode splitter to increase the isolation, because the double-ridge does not support the TE_{01} mode from port 1 in the square slot. The impedance matching at port 1 for the array element is realized by adjusting the length (L_p) of the probing tip of the coaxial and the position (D_p) of the feed point. Fig. 7 shows the simulated reflection coefficient with different values of L_p and D_p. When L_p = 2.8 mm and D_p = 2.7 mm, reflection coefficient of less than -11.5 dB is obtained from 17 GHz to 21.5 GHz. For port 2, the impedance matching is optimized by adjusting the height (H) and width (W) of the double-ridge waveguide-I. However, these two parameters

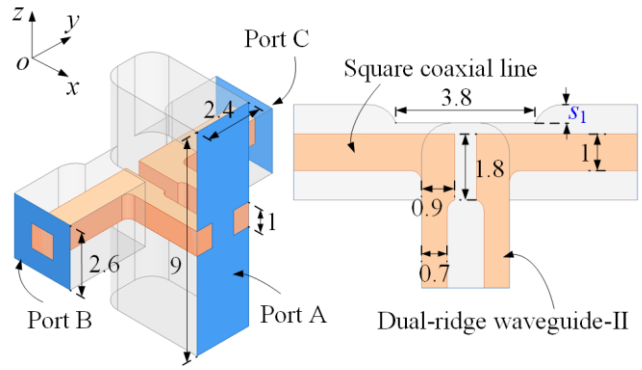

Fig. 10. Structure of the modified E-plane T-junction. All dimensions are given in millimeters.

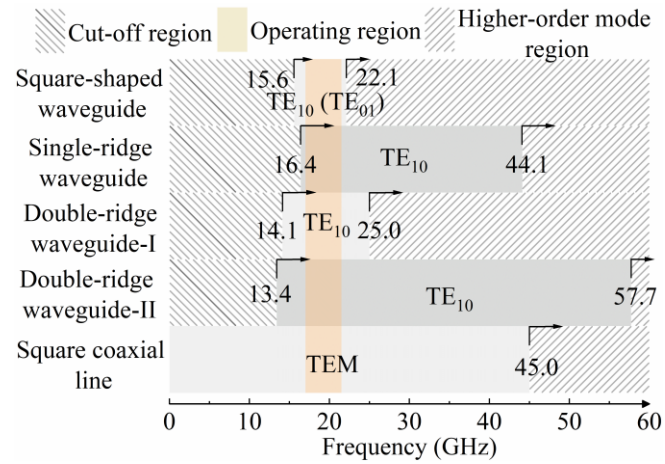

Fig. 11. Cut-off frequencies of all the involved transmission structures.

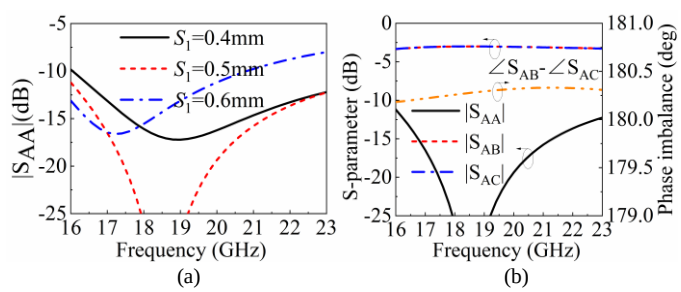

Fig. 12. Modified E-plane T-junctions. (a) $|S_{11}|$ with different values of S_1; (b) amplitude and phase responses of the final model.

also affect the isolation between ports 1 and 2. Therefore, a trade-off should be made after comprehensive consideration of both impedance matching and isolation. The parameter analysis on the impedance matching and isolation is shown in Fig. 8. When W = 6 mm, H = 3.9 mm, the reflection coefficients is less than -13.5 dB and the isolation is better than 38.5 dB from 17 GHz to 21.5 GHz. Fig. 9 plots the amplitude of the E-field within the array element when ports 1 and 2 are excited at 19.5 GHz, respectively. It shows how the E-field is coupled from the input port to the radiation slot. It also shows the de-coupling between port 1 and port 2, indicating a good port isolation.

B. Feed networks in Sub-array

1) H-pol feed network

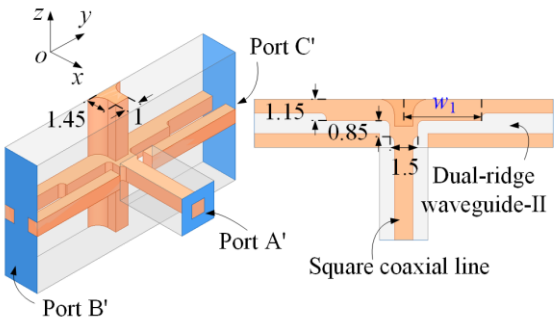

Fig. 13. Structure of the equal and in-phase T-junction. All dimensions are given in millimeters.

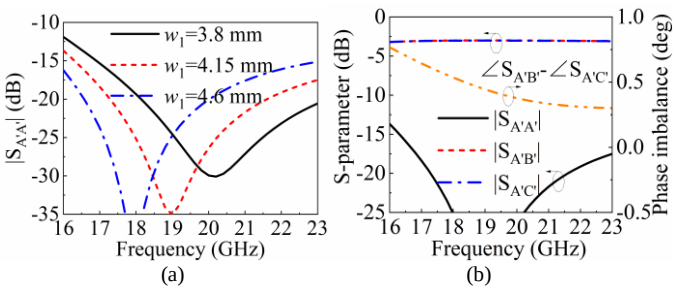

Fig. 14. The equal and in-phase T-junction. (a) $|S_{11}|$ with different values of w_1; (b) amplitude and phase responses of the final model.

Due to the limited distance between adjacent array elements, it is difficulty to place a full-corporate feed network excited from the same side. To overcome this issue, the array elements are excited back-to-back along *x*-direction based on a hybrid structure of the double-ridge waveguide and square coaxial line, as shown in Fig. 2(b). However, due to this mirror excitation, there is a 180° phase difference between the two back-to-back elements. To compensate for this phase difference, instead of using a coaxial junction (even mode), an E-plane double-ridge waveguide is used at the T-junction (odd mode) without requiring extra phase shifter. This is an important design feature. An enlarged view of this junction is further shown in Fig. 10. At the input (Port A) is a double-ridge waveguide. The outputs (Port B and C) are coaxial. Their center conductors are tapped to the two ridges, forming a transition from one TE10 to the two coaxial TEM modes. The tapped structures also serve to support the otherwise suspended center conductor. Based on the optimized dimensions shown in Figs. 3 and 10, Fig. 11 plots the electromagnetic (EM) modes of all feeding waveguides, including square-shaped waveguide, single-ridge waveguide, double-ridge waveguide-I, square coaxial line in array element, and double-ridge waveguide-II in the H-pol feed network. The square-shaped waveguide has narrowest fundamental mode bandwidth, but still well beyond the desired frequency band. The impedance matching is mainly achieved by adjusting the space between the inner and outer conductors in the coaxial branch. A parameter analysis of space S_1, defined in Fig 10, is shown in Fig. 12(a). $|S_{11}|$ is under -15 dB over 17-21.5 GHz, when S_1= 0.5 mm. Fig. 12(b) plots the simulated amplitude and phase responses of the final E-plane T-junction. The reflection coefficients for all ports are less than -15 dB, and balanced division of -3±0.2 dB is obtained. The phase difference between the output ports is 180°±0.4°.

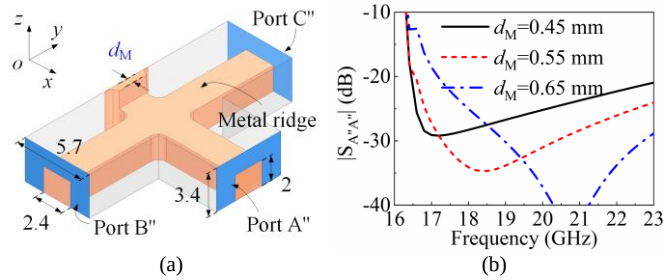

Fig. 15. Structure and simulated results of the basic H-plane T-junction in V-pol 1-to-4 power divider. (a) Structure; (b) Simulated $|S_{A''A''}|$ with different values of d_M. All dimensions are given in millimeters.

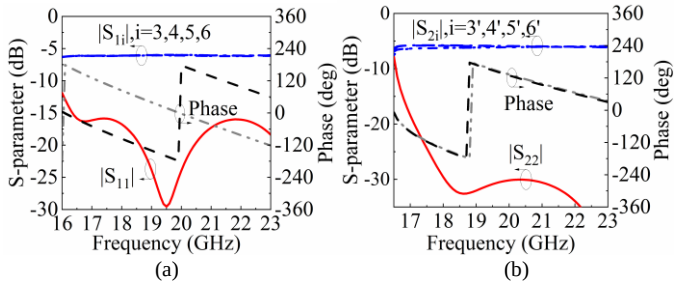

Fig. 16. Simulated S-parameters of (a) H- and (b) V-pol 1-to-4 power dividers.

Next, we will look at the main junction for the 1-to-4 divider as shown in Fig. 13. The input is a square coaxial line, whereas the outputs are connected to the double-ridge waveguide shown in Fig. 11. The inner conductor of coaxial line is attached to the centre of the junction for fixing. The impedance is matched by the stepped transformer structure. Fig. 14(a) shows the simulated reflection coefficient with different widths (w_1), defined in Fig. 13. An optimal impedance matching can be realized when w_1= 4.15 mm. The simulated amplitude and phase responses is plotted in Fig. 14(b). The reflection coefficients are all below -18 dB. The power division is -3±0.1 dB and output phase difference is ±1°.

2) V-pol feed network

The V-pol 1-to-4 power divider, shown in Fig. 2(c) is more straightforward in design. The output ports are all equal-amplitude and in-phase. The feed network is composed of three single-ridge H-plane T-junctions. The cut-off frequencies of all the involved transmission structures are shown in Fig. 11. Compared with the double-ridge waveguide-II and the square coaxial line, the single-ridge waveguide has the highest cut-off frequency. To minimize the size, the starting frequency of the concerned frequency band in this design is chosen to be as close to this highest cut-off frequency as possible. The basic junction is shown in Fig. 15(a). The impedance can be matched by adjusting the thickness (d_M) of the loaded metal plate at the center of the T-junction. Fig. 15(b) shows the optimal performance can be achieved when d_M = 0.55 mm.

The simulated S-parameters of the whole H- and V-pol 1-to-4 power dividers are illustrated in Fig. 16. Refer to Fig. 2 for the definition of port numbers 3(3'), 4(4'), 5(5') and 6(6'). Desired amplitude and phase distributions are achieved. Fig. 17

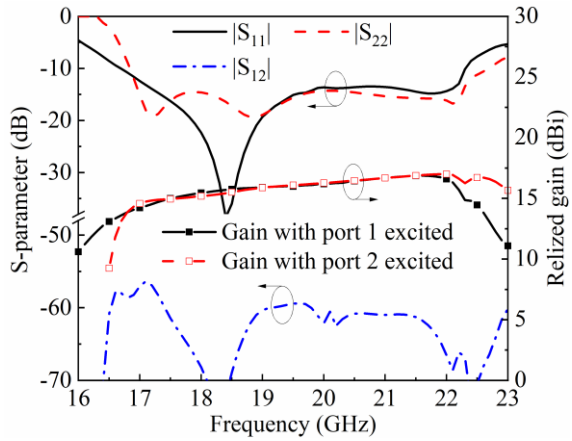

Fig. 17. Simulated S-parameters and peak gain of the optimized element for different polarizations.

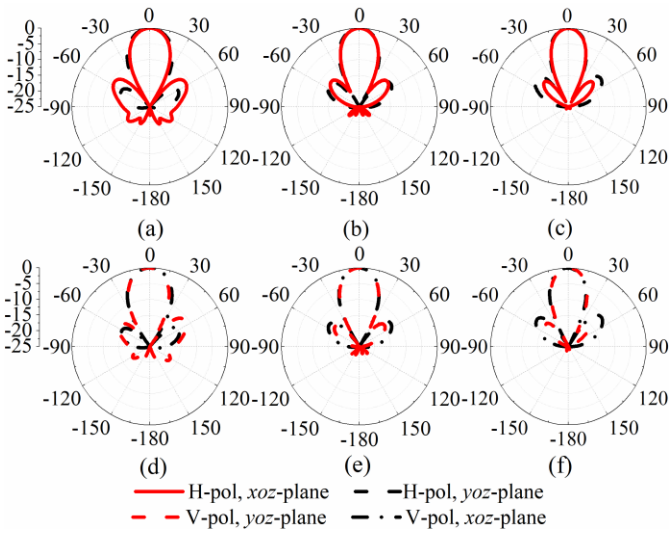

Fig. 18. Simulated radiation patterns of the optimized sub-array. (a) 17 GHz, H-pol; (b) 19.5 GHz, H-pol; (c) 21.5 GHz, H-pol; (d) 17 GHz, V-pol; (e) 19.5 GHz, V-pol; (f) 21.5 GHz, V-pol.

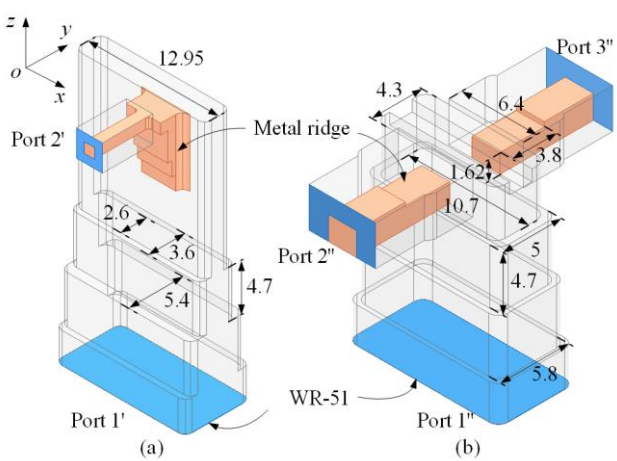

Fig. 19. Transition structures from standard WR-51 waveguide port to (a) square coaxial line and (b) single-ridge waveguide. All dimensions are given in millimeters.

shows the simulated S-parameters and peak gains of the optimized sub-array for different polarizations. In the desired frequency range of 17- 21.5 GHz, the reflection coefficients are below -12.4 dB and the isolation is better than 55 dB. The peak

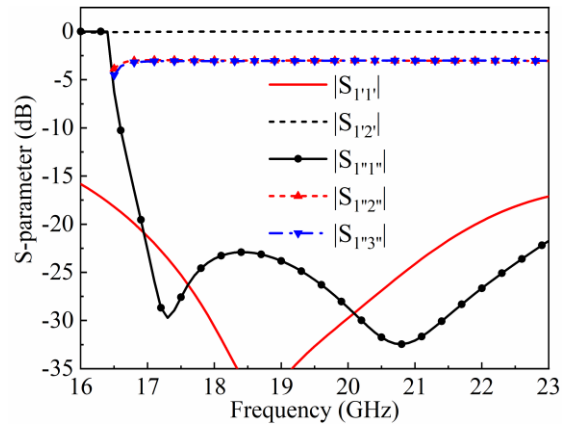

Fig. 20. Simulated S-parameters of the two transition structures in Fig. 19.

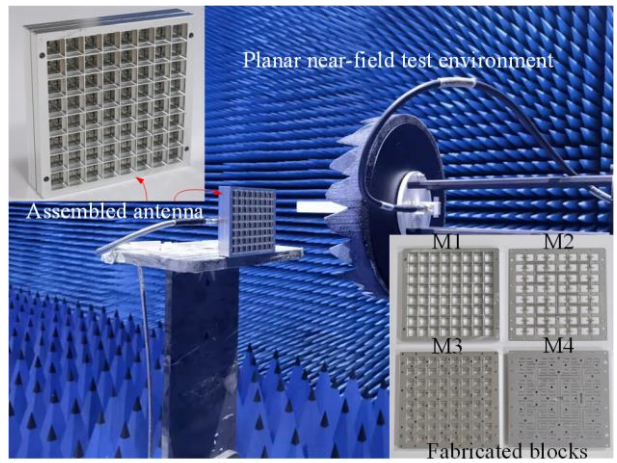

Fig. 21. Photographs of fabricated blocks, assembled antenna and test environment.

gains are consistent between the two polarizations and vary from 14.2 dBi to 16.8 dBi for H-pol and V-pol, respectively. Fig. 18 shows the simulated radiation patterns at 17, 19.5 and 21.5 GHz. The patterns for H-pol and V-pol match each other in the operating frequency band. They are symmetric both in *xoz*- and *yoz*-planes. The XPD of the sub-array is more than 34 dB.

C. Complete Array Antenna

The whole 8×8-element array antenna is constructed out of 16 sub-arrays. The two sets of feed networks are extended from their respective power dividers in the sub-array, as shown in Fig. 1(b). The inputs are standard WR-51 waveguide, so transition structures to the square coaxial line (for H-pol) and the single-ridge waveguide (V-pol) are required. They are both realized using multi-stepped rectangular waveguide transformers as shown in Fig. 19. The simulated reflection and transmission coefficients are plotted in Fig. 20. Good matching and low insertion loss have been achieved.

IV. Experimental Verification

The prototype is manufactured out of four metal layers, as marked out in Fig. 1. The blocks M1, M3 and M4 are CNC milled from aluminum-magnesium alloy with a tolerance of 20 μm. The type of the involved aluminum-magnesium alloy is 6061, and the nominal conductivity of 3.8×10^{7} S/m is used in the simulation. The thin layer M2 is cut by laser based on the

TABLE I
NORMALIZED RADIATION PATTERNS OF THE DUAL-POLARIZED ARRAY ANTENNA

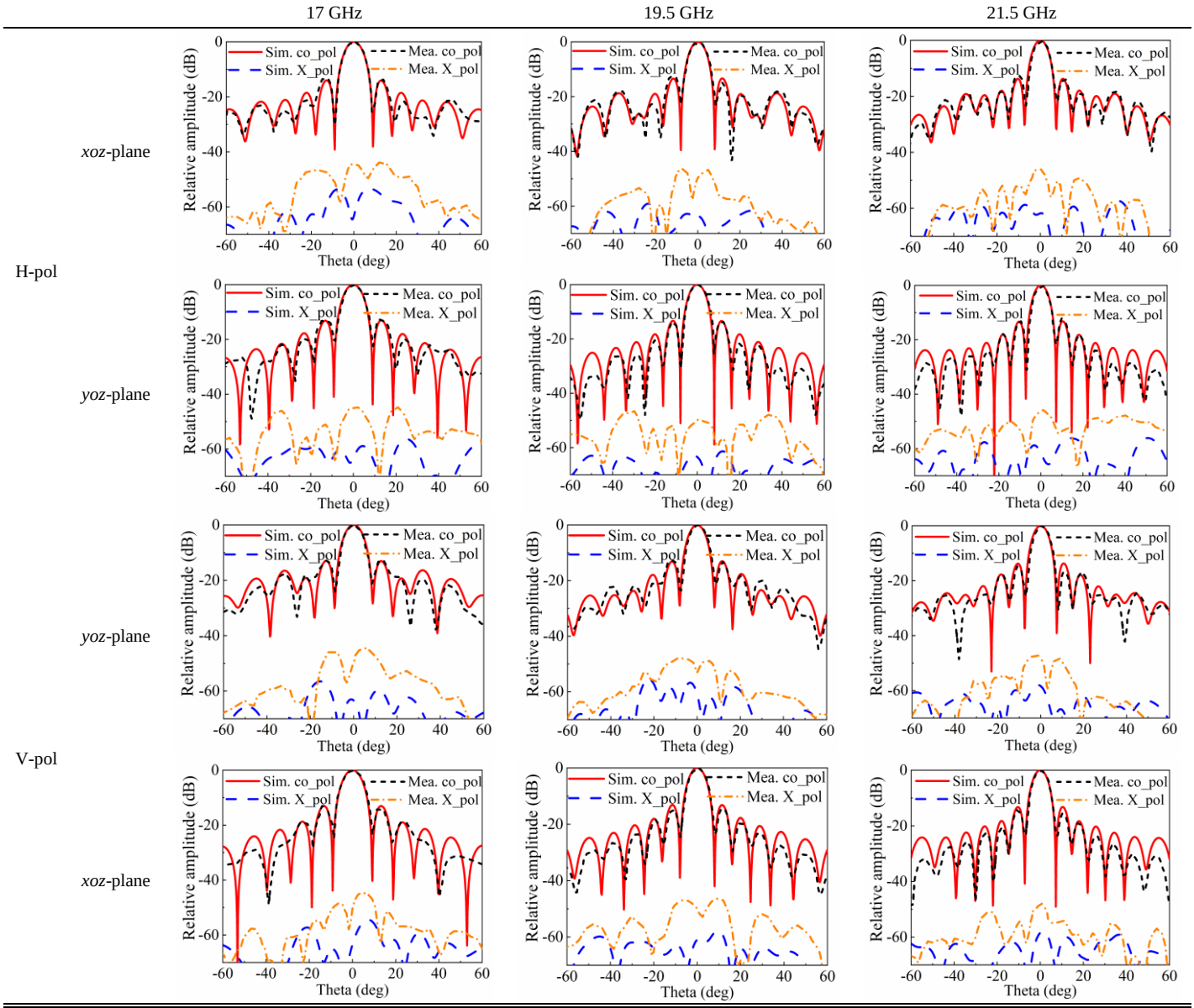

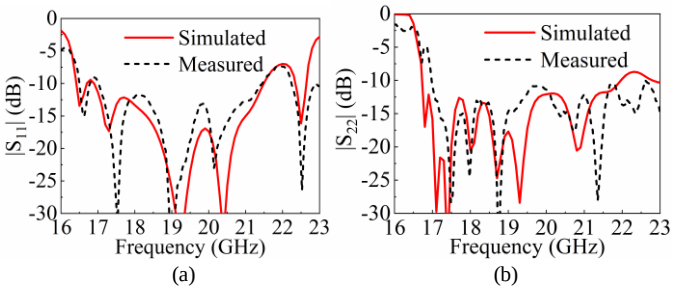

Fig. 22. Simulated and measured reflection coefficients. (a) H-pol; (b) V-pol.

same aluminum-magnesium alloy. Plenty of metal screws are installed around the feeding and radiating parts to ensure tight contact and suppress electromagnetic leakage. The separate metal blocks, the assembled dual-polarized antenna and the test environment are shown in Fig. 21. The prototype is 120 mm × 120 mm × 26.2 mm in size (with an aperture of 109.6 mm × 109.6 mm). The radiation measurement is conducted by using a near-field vertical planar scanner system from NSI-MI Technologies. The reflection coefficient and isolation are taken from an Agilent E8361C network analyzer.

A. Reflection Coefficient and Isolation

The simulated and measured H- and V-pol reflection coefficients are potted in Fig. 22(a) and (b). Good agreement has been shown. The simulated fractional bandwidth ($|S_{11}|$<-10 dB) is 24.0% (16.9 – 21.5 GHz) and 27.4% (16.7 – 22.0 GHz) for H- and V-pol, respectively. The measured FBW is 23.4% (17.0 – 21.5 GHz) for H-pol and 25.6 % (17.0 – 22.0 GHz) for V-pol. Fig. 23(a) shows the measured isolation is better than 51.2 dB over the desired frequency band. Fig. 23(b) shows the measured XPD is better than 43.6 dB.

TABLE II
PERFORMANCE COMPARISON OF HW-BASED FULL-CORPORATE-FEED DUAL-POLARIZED ANTENNAS

Ref.	Element type	Number of slots	Center frequency (GHz)/ FBW (%)	Gain (dBi)	Antenna efficiency (%)	Aperture efficiency (%)	XPD (dB)	Isolation (dB)	Aperture size (λ_0^2) [1]	Grating lobe suppression
[35]	Cross-shaped slot	16×16	62/10.9	32.2	80	90	-28	50	12.9×12.9	-20
[36]	Square-shaped slot	16×16	13.5/17.1	30.5	70	--	-28	39.5	11.3×11.3	-20
[37]	ME dipole	8×8	33.5/26.3	26.5	90	60	-30	36	8.6×8.6	-13
[39]	Circular-shaped slot	8×8	30.25/5.0	27.2	80	--	-50	50	--	--
This work	Square-shaped slot	8×8	19.25/23.4	26.8	83	90	-43.6	51.2	7.0×7.0	-18.1

[1] λ_0 is the free space wavelength at the center frequency of each passband.

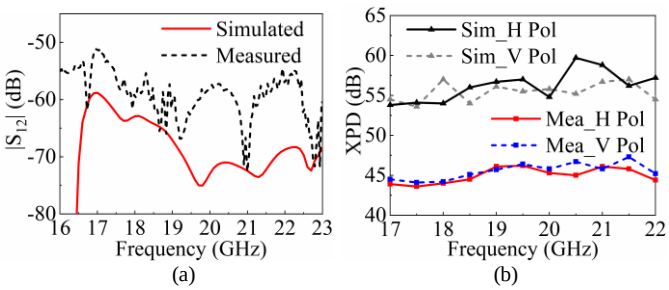

Fig. 23. Simulated and measured (a) port isolation and (b) XPD.

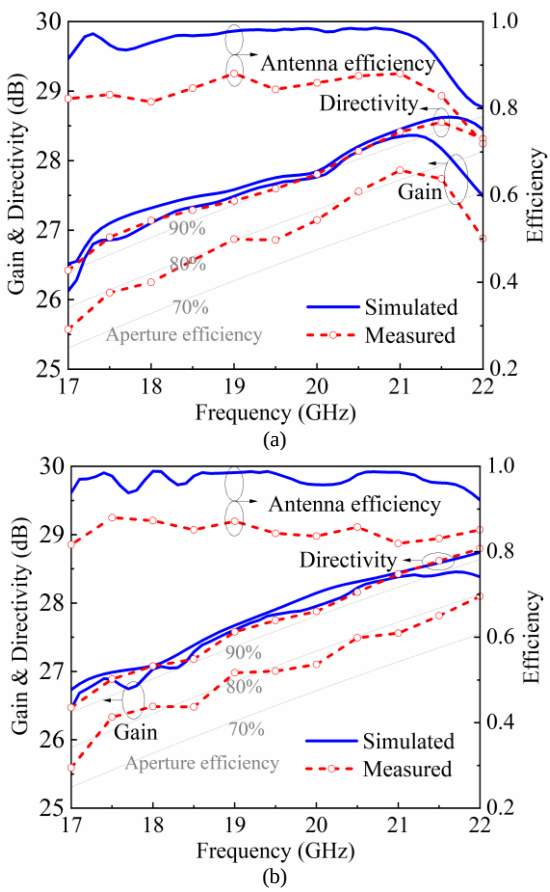

Fig. 24. Simulated and measured antenna peak gain and efficiency: (a) H- pol; (b)V-pol.

B. Radiation patterns and Efficiency

Table I shows the simulated and measured normalized radiation patterns at 17, 19.5, and 21.5 GHz. The patterns are stable across the frequency band and agree well with the simulation. The characteristics for the two polarizations are consistent. The 3-dB beamwidths in both *xoz*- and *yoz*-planes for H- and V-pol are over 6.4° from 17 GHz to 21.5 GHz. Thanks to the optimized height of the square-shaped slot (discussed in Section II-B), the measured grating lobes in *xoz*-plane for H-pol are suppressed across the same frequency range. The SLLs are around -13.1 dB, which is expected from a square array excited by constant amplitude and phase.

The simulated and measured peak gain and antenna efficiency are plotted in Fig. 24. The measured peak gains vary from 25.6 to 27.9 dBi and 25.5 to 27.8 dBi for H- and V-pol, while the simulated values are within the range of 26.1 - 28.4 dBi and 26.4 - 28.5 dBi. The small difference of about 0.6 dB is mainly caused by the fabrication tolerance, assemble and measurement errors. The measured directivities are 26.4 – 28.6 dBi and 26.5 – 28.8 dBi for H-pol and V-pol. The measured antenna and aperture efficiencies are better than 81.5% and 90.0% for both polarizations. The measured antenna efficiency and aperture efficiency are calculate by using the following equations:

$$\eta_{mea\_an} = \frac{G_{mea}}{D_{mea}} \tag{1-1}$$

$$\eta_{mea\_ap} = \frac{D_{mea}\lambda^2}{4\pi A} \tag{1-2}$$

Where, η_{mea_an} is the measured antenna efficiency, η_{mea_ap} is the measured aperture efficiency, G_{mea} is the measured peak gain, D_{mea} is the measured directivity, λ is the free-space wavelength corresponding to the operating frequency, A is the aperture area of the antenna. Both the measured peak gain and directivity can be directly obtained by using a near-field vertical planar scanner system from NSI-MI Technologies.

C. Comparison

Table II compares this work with other published HW-based dual-polarized antennas. [35]-[37] employed 1-to-4 backed cavity to excite their 2×22×2-element sub-arrays. Although [37] achieved an extended bandwidth of 26.3%, unwanted high grating lobe occurred. Only 16% bandwidth achieved with high level of grating lobe suppression. [39] removed the backed cavity layer and achieved a good radiation performance. However, due to relatively large space between the radiation slots, the FBW is only about 5%. With the new array topology and wideband response of the feed network, this work exhibits the largest FBW of 23.4% with grating lobe suppression. The antenna also shows stable radiation patterns, high antenna efficiency and low XPD within the frequency band.

V. Conclusion

In this paper, a HW-based wideband high-performance dual-polarized slot array antenna was demonstrated. Two sets of wideband full-corporate-feed networks are implemented for dual-polarization using two different structures. The upper feed network adopted a hybrid power division network of coaxial and double-ridge waveguide using both in-phase and out-of-phase T-junctions. The lower feed network, based on double-ridge waveguide structure instead, also serves as the orthogonal model splitter for isolation enhancement. This novel feeding topology facilitates the routing of the feeding network, thereby minimizing the distance between radiation slots to less than one free-space wavelength at the highest operating frequency. A prototype is implemented by using CNC milling and laser cutting. Measurement agrees well with the simulation, validating the design concept. Experimental results show that the peak gain is better than 25.5 dBi and antenna efficiency is higher than 81.5% over the frequency range of 17-21.5 GHz. The isolation and XPD are over 51.2 dB and 43.6 dB across the same frequency band. The wideband and dual-polarization make this design a good candidate for high data rate wireless applications such as satellite and 5G millimeter-wave communications.

References

[1] L. Chettri and R. Bera, "A comprehensive survey on internet of things (IoT) toward 5G wireless systems," *IEEE Internet Things J*, vol. 7, no. 1, pp. 16-32, Jan. 2020.

[2] A. Taha, Q. Qu, S. Alex, P. Wang, W. L. Abbott and A. Alkhateeb, "Millimeter wave MIMO-based depth maps for wireless virtual and augmented reality," *IEEE Access*, vol. 9, pp. 48341-48363, 2021.

[3] C. Deng et al., "IEEE 802.11be Wi-Fi 7: New challenges and opportunities," *IEEE Commun. Surveys Tuts.*, vol. 22, no. 4, pp. 2136–2166, 4th Quart., 2020.

[4] L. H. Ye, Y. F. Cao, X. Y. Zhang, Y. Gao and Q. Xue, "Wideband dual-polarized omnidirectional antenna array for base-station applications," *IEEE Trans. Antennas Propag.*, vol. 67, no. 10, pp. 6419-6429, Oct. 2019.

[5] Y. Liu, Z. Yue, Y. Jia, Y. Xu and Q. Xue, "Dual-band dual-circularly polarized antenna array with printed ridge gap waveguide," *IEEE Trans. Antennas Propag.*, vol. 69, no. 8, pp. 5118-5123, Aug. 2021.

[6] Y. Cai et al., "Dual-band circularly polarized transmitarray with single linearly polarized feed," *IEEE Trans. Antennas Propag.*, vol. 68, no. 6, pp. 5015-5020, Jun. 2020.

[7] L. Shen, H. Wang, W. Lotz and H. Jamali, "Compact dual polarization 4×4 MIMO multi-beam base station antennas," in *Proc. IEEE Int. Symp. Antennas Propag. USNC/URSI Nat. Radio Sci. Meeting*, 2018, pp. 1291-1292

[8] W. Sun, Y. Li, L. Chang, H. Li, X. Qin and H. Wang, "Dual-band dual-polarized microstrip antenna array using double-layer gridded patches for 5G millimeter-wave applications," *IEEE Trans. Antennas Propag.*, vol. 69, no. 10, pp. 6489-6499, Oct. 2021.

[9] A. Li and K. Luk, "Millimeter-wave dual linearly polarized endfire antenna fed by 180° hybrid coupler," *IEEE Antennas Wireless Propag. Lett.*, vol. 18, no. 7, pp. 1390-1394, Jul. 2019.

[10] C. Sim, C. Chang and J. Row, "Dual-feed dual-polarized patch antenna with low cross polarization and high isolation," *IEEE Trans. Antennas Propag.*, vol. 57, no. 10, pp. 3321-3324, Oct. 2009.

[11] P. Kumar, S. Dwari, R. K. Saini and M. K. Mandal, "Dual-band dual-sense polarization reconfigurable circularly polarized antenna," *IEEE Antennas Wireless Propag. Lett.*, vol. 18, no. 1, pp. 64-68, Jan. 2019.

[12] W. Li, X. Tang and Y. Yang, "Design and implementation of SIW cavity-backed dual-polarization antenna array with dual high-order modes," *IEEE Trans. Antennas Propag.*, vol. 67, no. 7, pp. 4889-4894, Jul. 2019.

[13] G. Srivastava and A. Mohan, "A differential dual-polarized SIW cavity-backed slot antenna," *IEEE Trans. Antennas Propag.*, vol. 67, no. 5, pp. 3450-3454, May 2019.

[14] P. Li, S. Liao, Q. Xue and S. Qu, "60 GHz dual-polarized high-gain planar aperture antenna array based on LTCC," *IEEE Trans. Antennas Propag.*, vol. 68, no. 4, pp. 2883-2894, Apr. 2020.

[15] W. Zhao, X. Li, Z. Qi and H. Zhu, "Broadband and high gain dual-polarized antenna array with shared vias feeding network for 5G applications," *IEEE Antennas Wireless Propag. Lett.*, vol. 20, no. 12, pp. 2377-2381, Dec. 2021.

[16] L. Zhang et al., "Wideband 45° linearly polarized slot array antenna based on gap waveguide technology for 5G millimeter-wave applications," *IEEE Antennas Wireless Propag. Lett.*, vol. 20, no. 7, pp. 1259-1263, Jul. 2021.

[17] Y. You, Y. Lu, T. Skaik, Y. Wang and J. Huang, "Millimeter-wave 45° linearly polarized corporate-fed slot array antenna with low profile and reduced complexity," *IEEE Trans. Antennas Propag.*, vol. 69, no. 9, pp. 6064-6069, Sep. 2021.

[18] M. Ferrando-Rocher, J. I. Herranz-Herruzo, A. Valero-Nogueira and B. Bernardo-Clemente, "Dual circularly polarized aperture array antenna in gap waveguide for high-efficiency Ka-band satellite communications," *IEEE Open J. Antennas Propag.*, vol. 1, pp. 283-289, 2020.

[19] G. Mishra, S. K. Sharma, J. -C. Chieh, R. Olsen and P. Nguyen, "Ku-band dual linear polarized parabolic-cylindrical reflector antenna with beam steering performance," in International Applied Computational Electromagnetics Society Symposium (ACES), Monterey, CA, 2020, pp. 1-2

[20] Z. Zhang, Y. Zhao, N. Liu, L. Ji, S. Zuo and G. Fu, "Design of a dual-beam dual-polarized offset parabolic reflector antenna," *IEEE Trans. Antennas Propag.*, vol. 67, no. 2, pp. 712-718, Feb. 2019.

[21] S. Mener, R. Gillard, R. Sauleau, A. Bellion and P. Potier, "Dual circularly polarized reflectarray with independent control of polarizations," *IEEE Trans. Antennas Propag.*, vol. 63, no. 4, pp. 1877-1881, Apr. 2015.

[22] C. S. Geaney, M. Hosseini and S. V. Hum, "Reflectarray antennas for independent dual linear and circular polarization control," *IEEE Trans. Antennas Propag.*, vol. 67, no. 9, pp. 5908-5918, Sep. 2019.

[23] J. Yin, Q. Lou, H. Wang, Z. N. Chen and W. Hong, "Broadband dual-polarized single-layer reflectarray antenna with independently controllable 1-bit dual beams," *IEEE Trans. Antennas Propag.*, vol. 69, no. 6, pp. 3294-3302, June 2021.

[24] D. R. Prado, M. Arrebola, M. R. Pino and G. Goussetis, "Contoured-beam dual-band dual-linear polarized reflectarray design using a multiobjective multistage optimization," *IEEE Trans. Antennas Propag.*, vol. 68, no. 11, pp. 7682-7687, Nov. 2020.

[25] M. Akbari, A. Farahbakhsh and A. Sebak, "Ridge gap waveguide multilevel sequential feeding network for high-gain circularly polarized array antenna," *IEEE Trans. Antennas Propag.*, vol. 67, no. 1, pp. 251-259, Jan. 2019.

[26] M. Akbari et al., "Highly efficient 30 GHz 2x2 beamformer based on rectangular air-filled coaxial line," *IEEE Trans. Antennas Propag.*, vol. 68, no. 7, pp. 5236-5246, July 2020.

[27] M. Farahani, M. Akbari, M. Nedil, A. -R. Sebak and T. A. Denidni, "Millimeter-wave dual left/right-hand circularly polarized beamforming network," *IEEE Trans. Antennas Propag.*, vol. 68, no. 8, pp. 6118-6127, Aug. 2020.

[28] M. Sano, J. Hirokawa and M. Ando, "Single-layer corporate-feed slot array in the 60-GHz band using hollow rectangular coaxial lines," *IEEE Trans. Antennas Propag.*, vol. 62, no. 10, pp. 5068-5076, Oct. 2014.

[29] T. Lou, X. Yang, H. Qiu, Z. Yin and S. Gao, "Compact dual-polarized continuous transverse stub array with 2-D beam scanning," *IEEE Trans. Antennas Propag.*, vol. 67, no. 5, pp. 3000-3010, May 2019.

[30] M. Śmierzchalski et al., "A novel dual-polarized continuous transverse stub antenna based on corrugated waveguides—part II: experimental demonstration," *IEEE Trans. Antennas Propag.*, vol. 69, no. 3, pp. 1313-1323, Mar. 2021.

[31] X. Lu, H. Zhang, S. Gu, H. Liu, X. Wang and W. Lu, "A dual-polarized cross-slot antenna array on a parallel-plate waveguide with compact

structure and high efficiency," *EEE Antennas Wireless Propag. Lett.*, vol. 17, no. 1, pp. 8-11, Jan. 2018.

[32] Y. Chen and R. G. Vaughan, "Dual-polarized L-band and single-polarized X-band shared-aperture SAR array," *IEEE Trans. Antennas Propag.*, vol. 66, no. 7, pp. 3391-3400, Jul. 2018.

[33] J. Lu et al., "Broadband dual-polarized waveguide slot filtenna array with low cross polarization and high efficiency," *IEEE Trans. Antennas Propag.*, vol. 67, no. 1, pp. 151-159, Jan. 2019.

[34] M. Chen, X. -C. Fang, W. Wang, H. -T. Zhang and G. -L. Huang, "Dual-band dual-polarized waveguide slot antenna for SAR applications," *IEEE Antennas Wireless Propag. Lett.*, vol. 19, no. 10, pp. 1719-1723, Oct. 2020.

[35] D. Kim, M. Zhang, J. Hirokawa and M. Ando, "Design and fabrication of a dual-polarization waveguide slot array antenna with high isolation and high antenna efficiency for the 60 GHz band," *IEEE Trans. Antennas Propag.*, vol. 62, no. 6, pp. 3019-3027, Jun. 2014.

[36] S. Zhou, G. Huang, T. Chio, J. Yang and G. Wei, "Design of a wideband dual-polarization full-corporate waveguide feed antenna array," *IEEE Trans. Antennas Propag.*, vol. 63, no. 11, pp. 4775-4782, Nov. 2015.

[37] F. Sun et al., "A millimeter-wave wideband dual-polarized antenna array with 3-D-printed air-filled differential feeding cavities," *IEEE Trans. Antennas Propag.*, vol. 70, no. 2, pp. 1020-1032, Feb. 2022.

[38] I. Nistal-González et al., "Planar phased array antenna for nomadic satellite communication in Ka-band," in *Proc. 11th Eur. Radar Conf.*, Oct. 2014, pp. 396–399.

[39] M. Ferrando-Rocher, J. I. Herranz-Herruzo, A. Valero-Nogueira, B. Bernardo-Clemente, A. U. Zaman and J. Yang, "8×8 Ka-band dual-polarized array antenna based on gap waveguide technology," *IEEE Trans. Antennas Propag.*, vol. 67, no. 7, pp. 4579-4588, Jul. 2019.